

Contents

2	1 Diamond irradiation study	3
3	1.1 Measurement setup	4
4	1.1.1 Preamplifiers	4
5	1.1.2 Diamond samples	6
6	1.1.3 Readout devices	7
7	1.1.4 Setup for the β detection efficiency study	7
8	1.1.5 Room temperature α -TCT setup	8
9	1.1.6 Cryogenic α -TCT setup	8
10	1.2 Charged particle pulses and spectra	9
11	1.3 Radiation limitations	12
12	1.3.1 Irradiation study	12
13	1.3.2 Long-term measurement stability	13
14	1.4 Temperature limitations	22
15	1.4.1 Temperature-variant α -TCT before irradiation	22
16	1.4.2 Temperature-variant α -TCT after irradiation	24
17	1.5 Conclusion	29

¹⁸ **Chapter 1**

¹⁹ **Diamond irradiation study**

²⁰ The aim of the study in this chapter is to find the operational limitations of diamond
²¹ detectors for spectroscopy and tracking applications. The chapter contains the measurement
²² results of data taken with diamond sensors. First the measurement setup is described in
²³ section 1.1. Then the measured particle spectra are shown in 1.2. This is followed by a
²⁴ study of effects of the irradiation damage on the electrical signal of the diamond detector.
²⁵ The last section shows the results of the measurements of irradiated diamond samples at
²⁶ cryogenic temperatures. The studies compare the experimentally acquired data with the
²⁷ theory from the previous chapter and define limitations of the diamond detectors in terms
²⁸ of radiation and temperature.

²⁹ Diamond sensors are mainly used for two types of measurements: particle counting and
³⁰ spectroscopy. The first type of measurements depends on the sensor efficiency – its ability to
³¹ detect all or at least a known percentage of incident particles. The energy of the particles is
³² not so important; what bears the information is the rate and the spatial distribution. Here
³³ the particles do not necessarily stop in the bulk – they exit the sensor with a slightly lower
³⁴ energy. In spectroscopy, on the other hand, the particles stop within the sensor, depositing
³⁵ all their energy. This energy is then measured by collecting the freed charge carriers. The
³⁶ goal of the experiments described in this chapter is to:

- ³⁷ 1. Quantify the efficiency of the sCVD diamond in counting mode,
- ³⁸ 2. Quantify the degradation of the efficiency as a function of fluence,
- ³⁹ 3. Quantify the macroscopic effects on charge carrier behaviour as a function of the
fluence and
- ⁴¹ 4. Define limitations for use in spectroscopy.

⁴² The results discussed here show that there are several limitations for using diamond as
⁴³ a radiation detector. All of them need to be taken into account when designing a new
⁴⁴ measurement device. The irradiation study allows for an estimation of the lifetime of the
⁴⁵ detector and a prediction of the longterm signal degradation as a function of fluence. The
⁴⁶ result of the study is a correction factor, which can be applied during data analysis to ensure
⁴⁷ that the analysis results are stable despite the detector degradation.

1.1. MEASUREMENT SETUP

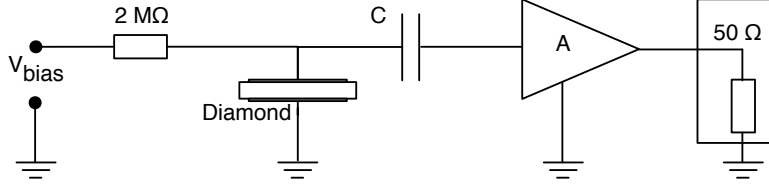


Figure 1.1: Diagram of a diamond detector readout chain.

48 1.1 Measurement setup

49 The first step of designing a measurement setup is to define the measurement conditions,
50 such as the temperature, the type of radiation and its flux. The second step is to ensure
51 that the setup is insensitive to external electromagnetic interferences and that it minimises
52 electrical noise in the system. The setup needs to be calibrated before use.

53 The measurements using diamond that are explained in these chapters have been carried
54 out using several measurement setups, but they are all similar in terms of the electrical
55 signal chain. The measurement chain consists of three main parts: a diamond sensor, a
56 signal preamplifier and a readout device, as seen in figure 1.1. The signals propagating
57 along the analogue chain are fast – in the GHz bandwidth range – and with low amplitudes
58 – of the order of tens of μV . This gives rise to the importance of shielding from external
59 radio-frequency (RF) interferences. Also, the carrier and the preamplifier have to have a
60 matched impedance. Finally, the system needs to be grounded properly.

61 1.1.1 Preamplifiers

62 Two preamplifiers are used for the measurements, one sensitive to charge and the other
63 to current. *CIVIDEC Cx* (figure 1.2a) is a charge sensitive amplifier. Its high SNR is
64 achieved due to a low equivalent noise charge of 300 e^- with an additional 30 e^- per each
65 pF of the sensor capacitance. A reported gain of $\sim 12 \text{ mV/fC}$ makes it a good choice for
66 spectroscopic measurements with diamond sensors. *CIVIDEC C2* (figure 1.2b) is a fast
67 current preamplifier with a 2 GHz bandwidth limit. It is used for TCT measurements
68 because of its fast response and a good SNR. Both are embedded in an RF-tight aluminium
69 box to reduce the noise pickup. Both have an AC coupled input and a 50Ω output.

70 A 2 GHz bandwidth limit defines the minimum rising time equal to $t_r \simeq \frac{0.34}{BW} = \frac{0.34}{2 \times 10^9} =$
71 170 ps, therefore the system with a CIVIDEC C2 amplifier is capable of measuring pulses
72 with a minimum FWHM $\simeq 170 \text{ ps}$. The initial peak in the α pulse has a lower FWHM;
73 for example, if a charge carrier travelling through the bulk takes $t_1 \sim 6 \text{ ns}$ to reach the
74 electrode on the opposite side ($d_1 \sim 500 \mu\text{m}$), the carrier with the opposite charge and a
75 shorter path to the closer electrode – max. $d_2 \sim 10 \mu\text{m}$ – only takes $t_2 \sim \frac{d_2}{d_1} t_1 = 120 \text{ ps}$.
76 Such a short drift time induces a current pulse that is too narrow for the system to detect.

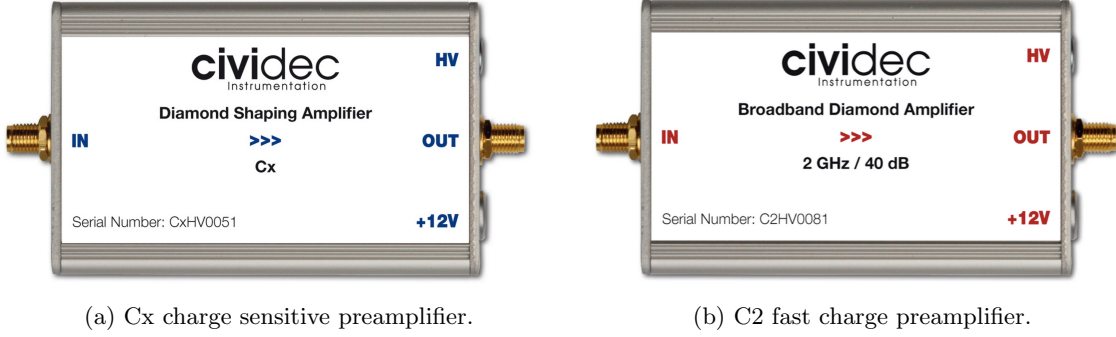


Figure 1.2: Amplifiers used for the charge and current measurements.

77 Calibration

78 The amplifiers have to be calibrated before use to determine their gain. Both are calibrated
79 using a square signal generator with a known amplitude step of $U_{\text{in}} = (252 \pm 5)$ mV. A
80 2 GHz oscilloscope with a 10 GS/s sampling rate is used to carry out the calibration.

81 **Cx charge sensitive amplifier** calibration necessitates an injection of a well known charge.
82 Therefore the signal from a pulse generator is routed through a capacitor with a calibration
83 capacitance $C_{\text{cal}} = (0.717 \pm 0.014)$ pF and then to the input of the amplifier. The pulse
84 area behind the capacitor is $a_{\text{cal}} = (5.0 \pm 0.5)$ pVs, with the signal amplitude on the output
85 amounting to $U_{\text{Cx}} = (1.95 \pm 0.05)$ V. The input voltage step combined with the calibration
86 capacitance yields a calibration charge

$$Q_{\text{cal}} = C_{\text{cal}} \cdot U_{\text{in}} = (181 \pm 5) \text{ fC}. \quad (1.1)$$

87 The gain of the Cx amplifier when comparing the integrated input charge to the output
88 amplitude is

$$A_{\text{Cx}}^Q = \frac{U_{\text{Cx}}}{Q_{\text{cal}}} = (9.3 \pm 0.4) \text{ mV/fC} \quad (1.2)$$

89 whereas the factor between the area of the input current pulse and the output amplitude is

$$A_{\text{Cx}}^a = \frac{U_{\text{Cx}}}{a_{\text{cal}}} = (390 \pm 40) \text{ mV/pVs}. \quad (1.3)$$

90 The area-based amplification factor A_{Cx}^a can be used as an estimate for the integrated charge
91 of a current pulse. However, it has a higher uncertainty ($\sim 10\%$) than the amplitude-based
92 factor A_{Cx}^Q ($\sim 4\%$) due to the measurement limitations of the oscilloscope.

93 **C2 current amplifier** calibration only requires the measurement of the amplitude gain.
94 To keep the output signal amplitude within the ± 1 V linear range of the amplifier, the
95 input signal amplitude has to be minimised. The signal from the generator is therefore
96 routed through a 36 dB attenuator to decrease its amplitude to $U_{\text{inAtt}} = (3.95 \pm 0.05)$ mV.
97 Two amplifiers with different gains have been measured, because both are used for the

1.1. MEASUREMENT SETUP

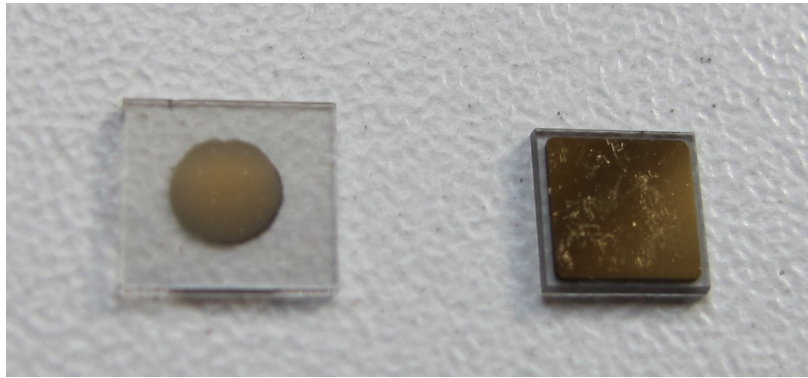


Figure 1.3: Two scCVD diamond samples: A IIa 1scdhq (left) and an E6 S37 (right).

98 measurements. The output of the first amplifier amounts to $U_{C2-1} = (860 \pm 5)$ mV. This
99 yields the amplification gain

$$100 \quad A_{C2-1} = \frac{U_{\text{inAtt}}}{U_{C2-1}} = (217 \pm 3). \quad (1.4)$$

100 The second amplifier has the output equal to $U_{C2-2} = (632 \pm 5)$ mV with the resulting gain
101 of $A_{C2-2} = (152 \pm 3)$.

102 1.1.2 Diamond samples

103 The sensor samples used for these studies have been acquired from Element Six (E6) [1].
104 They all have the same standard dimensions. sCVD diamonds with dimensions $4.7 \times$
105 4.7 mm^2 are already sufficiently large for most of the beam monitoring applications and
106 still affordable. One sample with dimensions of $5.6 \times 5.3 \text{ mm}^2$ produced by IIa Singapore [2]
107 has also been characterised at CERN [3]. The target thickness for all samples is 500 μm .
108 Diamonds this thick yield a high enough signal-to-noise ratio for MIPs to be measured
109 by the available electronics. Table 1.1 shows all the samples used for this study. Two of
110 them are measured before and after irradiation and then compared. Irradiation doses for
111 damaging the material need to be high – above 10^{12} particles per cm^2 to be able to observe
112 a significant change in behaviour of a diamond sensor.

Name	Type	Producer	Dimensions [mm^2]	Thickness [μm]	Electrode	Irradiated
S37	sCVD	E6	4.7×4.7	548	Cr/Au	no
S50	sCVD	E6	4.7×4.7	537	Cr/Au	no
S52	sCVD	DDL	4.7×4.7	515	DLC/Pt/Au	$3.6 \times 10^{14} \frac{\pi}{\text{cm}^2}$
S79	sCVD	E6	4.7×4.7	529	Cr/Au	$1 \times 10^{14} \frac{\pi}{\text{cm}^2}$
ELSC	sCVD	E6	4.7×4.7	491	Cr/Au	no
1scdhq	sCVD	IIa	5.6×5.3	460	Cr/Au	no

114 Table 1.1: Diamond sensor samples used.

115 The diamond samples have quoted impurity densities of $\leq 2 \times 10^{14} \text{ cm}^{-3}$ and nitrogen
116 incorporation of $\leq 10^{-9}$. The electrodes were added by various companies and institutes.

117 For instance, S52 was metallised by a company DDL (now defunct) while the Physics De-
118 partment of the University of Firenze, Italy metallised the S79. There are also several
119 techniques for producing the electrodes. The DDL contacts consist of three layers: DLC
120 (diamond-like carbon)/Pt/Au with 4/10/200 nm thicknesses, respectively. The metallisa-
121 tion for S79, on the other hand, is made up of Cr/Au with a total thickness of \sim 400 nm.
122 The area coverage also differs from sample to sample. Diamonds must not be metallised
123 until the very edge as the proximity of contacts with a high potential may lead to sparking.
124 However, the areas not covered by the metallisation are less efficient because the fringe
125 fields at the edges are not as strong as in between the electrodes. This effectively reduces
126 the sensitive area of the sensors. In the diamonds used here the effective area is anywhere
127 from 9 mm² to 18 mm². The leakage current is below 1 nA, but increases for the irradiated
128 samples. The capacitance is of the order of (2.0 \pm 0.3) pF.

129 1.1.3 Readout devices

130 Electrical signals in diamond detectors are in the GHz frequency range. To preserve the
131 information in the signals, the readout device with a high bandwidth limit must be used.
132 For instance, a 20 MHz limit is enough for the spectroscopic measurements with the Cx
133 charge amplifier, but is insufficient for the current measurements with the C2 amplifier.

134 Two devices are used take data shown in this chapter. The first choice is a 2 GHz LeCroy
135 WaveRunner 204MXi-A. This specific model has a sufficiently high bandwidth limit for the
136 fast current preamplifier signals. It offers a reliable solution for analogue signal readout of
137 limited amounts of data. However, its slow acquisition speed is a bottleneck in a test beam
138 experiment. Its initial 100 Hz readout rate decreases to a mere 20 Hz within 20 minutes,
139 because every single trigger is saved as a separate file and the Windows operating system
140 is not capable of handling 10000+ files in a single directory easily. This is why it has been
141 exchanged with a DRS4 [4], an analogue readout device developed by PSI, Switzerland.
142 This compact device is capable of recording up to four waveforms at a time at a steady
143 rate of up to 500 Hz. Its 700 MHz bandwidth limitation is sufficient for the signal from the
144 charge amplifier.

145 1.1.4 Setup for the β detection efficiency study

146 The efficiency study of the diamond sensors has been carried out at CERN in the North
147 Hall test beam facility. There a straight high-energy particle beam of 120 GeV π is provided
148 to the users to calibrate their detectors. The beam has a transverse spread of $\sigma = 10$ mm in
149 both axes. The particle rate is of the order of $10^4 \pi \text{ cm}^{-2} \text{ s}^{-1}$. A diamond sensor embedded
150 in a printed circuit board (PCB) carrier has been placed in the beam spot perpendicular
151 to the beam and connected via an SMA connector directly to a charge amplifier. The
152 amplified signal is read out using a LeCroy oscilloscope and a DRS4 analogue readout
153 system. A computer is used as a controller and data storage for the readout device. A
154 beam telescope is used as a reference detector. It is a device that helps to cross-check the
155 measurements of the devices under test (DUTs) and to carry out spatially resolved studies

1.1. MEASUREMENT SETUP

on the DUTs. It consists of several pixellated sensor planes placed in series, which can track a particle's trajectory with a precision of a few μm . The sensor planes are positioned in front of the DUT and behind it. Then the beam telescope acts as a trigger system – it triggers the readout of both the telescope data and DUT data when both the planes in front and behind the DUT record a hit by an incident particle. A particle detected by all the planes within the DUT window and the DUT itself counts towards its efficiency whereas a hit missed by the DUT means that the DUT is not 100 % efficient. To discard the hits that miss the DUT completely, a region of interest (ROI) can be chosen in the beam telescope planes. The equation for calculating the sensor efficiency is therefore

$$\epsilon = \frac{N_{\text{DUT}} \wedge N_{\text{telescope}}}{N_{\text{telescope}}} \quad (1.5)$$

for an ROI smaller than the sensitive region of the diamond.

1.1.5 Room temperature α -TCT setup

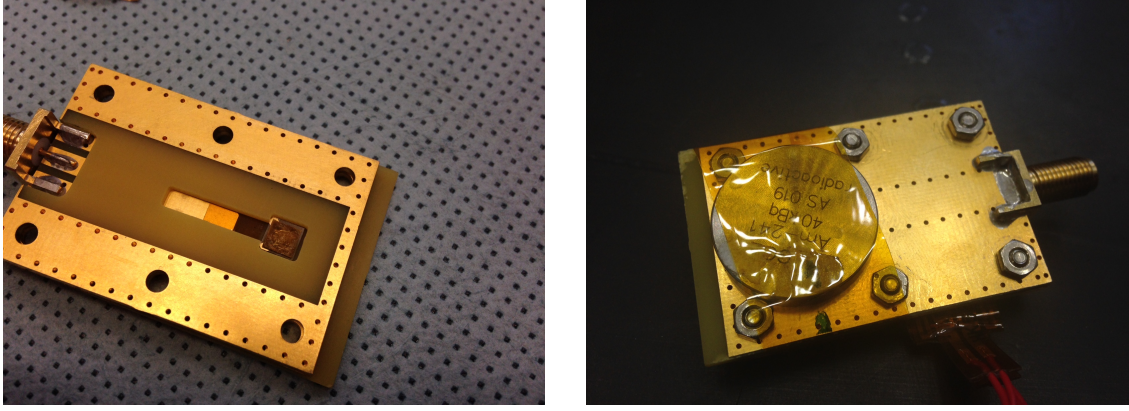
This TCT study is a follow-up of an extensive diamond TCT study at cryogenic temperatures [5]. The room-temperature TCT measurements have been carried out in the laboratory. The setup consists of a diamond sensor embedded in a PCB carrier, a current amplifier and an oscilloscope. To measure α particles, their energy loss during their trajectory has to be minimised. Therefore the diamond is placed inside a vacuum chamber. The chamber is a steel tube with a diameter of 5 cm. On one side it is connected to a vacuum pump via a steel hose. A feedthrough with an SMA connector is placed on the other side. A CIVIDEC C2 current amplifier is connected directly onto the feedthrough. The amplified output is connected to the oscilloscope via an SMA cable. An ^{241}Am source with a diameter of 2 cm and a height of 0.5 cm is fixed onto the sensor carrier (figure 1.4a, figure 1.4b). Then the carrier is inserted in the chamber and fixed in place using an air-tight clamp. The pump can then be switched on. It is capable of providing the inside pressure as low as 10^{-4} mbar after approximately one hour of operation.

1.1.6 Cryogenic α -TCT setup

The experiment at cryogenic temperatures has been carried out at the Central Cryogenic Laboratory at CERN. The room-temperature TCT setup has to be modified to allow for measurements at temperatures as low as 4 K. It consists of three parts:

1. a cryostat – a thermally insulated cylinder containing liquid helium,
2. an inlet – an air-tight mechanical tube with valves and feedthroughs at the top that is lowered in the liquid helium and
3. the diamond sample embedded in a PCB carrier with a fitted temperature sensor, a heater and cables leading to the feedthroughs.

The setup is described in detail in [5].



(a) PCB carrier with an embedded diamond sample. (b) Radioactive source over the carrier.

Figure 1.4: Positioning of the α -source on top of the sensor carrier.

When the diamond sample is placed in the PCB carrier and the ^{241}Am source is in place, the inlet is sealed and lowered in the empty cryostat. Then the inside volume of the inlet is evacuated down to 10^{-5} mbar while the liquid helium is flowing into the cryostat. To improve the thermal contact between the diamond and the coolant, a small amount of helium gas is added inside the evacuated inlet, setting the vacuum to around 10^{-3} mbar. This value changes with time, because the gas condenses on the walls of the inlet, reducing the number of floating particles. For this reason the helium gas has to be added on an irregular basis. Every addition causes a significant undershoot of the sample temperature, which has to be corrected for using a heater placed on the back of the PCB carrier. Also, the added gas deteriorates the vacuum inside the inlet. Furthermore, at approximately 60 K the helium gas has to be evacuated from the inlet to avoid a potential explosion due to the expansion of the gas with temperature.

When the sample is cooled to 4 K, the minimum temperature achievable by means of liquid helium without over-pressurising it, the measurements can begin. A temperature sensor placed on the back of the PCB carrier is used to measure the temperature of the sample. After every temperature data point, the current through the heater is increased, heating up the sample. The initial temperature time constant of the order of tenths of seconds at low temperatures increases with temperature. Even more so when helium is evacuated from the inlet at 60 K, removing the thermal bridge between the wall of the inlet and the diamond sample. At the room temperature (RT), the time constant is already of the order of minutes.

1.2 Charged particle pulses and spectra

In previous chapter the ionisation profiles for different types of radiation were discussed. β radiation induces a triangular electric pulse whereas α radiation induces a rectangular one. However, their amplitude, width and rise/fall time depend heavily on the type of interaction with the diamond, the purity of the diamond and the bandwidth of the amplifier

1.2. CHARGED PARTICLE PULSES AND SPECTRA

and the oscilloscope. This section shows the signal pulses of α , β and γ radiation with their respective energy distributions for the case of a diamond detector.

Figure 1.5 shows a set of pulses and an averaged waveform for 5.5 MeV α , 2.3 MeV β and 1.3 MeV γ radiation using an ^{241}Am , a ^{90}Sr and a ^{60}Co source, respectively. The particles are measured with the non-irradiated sCVD diamond S37. α particles always produce the same signal pulse with a noise RMS of 2.7 mV. The averaging suppresses the noise while retaining most the information. It does, however, smear the rising and falling edge, increasing the rising and falling time. Theta_r is now of the order of 0.5 ns. Both β and γ pulses look similar - triangular and with a wide range of amplitudes. Here the pulse count is low, so the pulses with a high amplitude are not recorded. A trigger would need to be set very high to “catch” them with the oscilloscope.

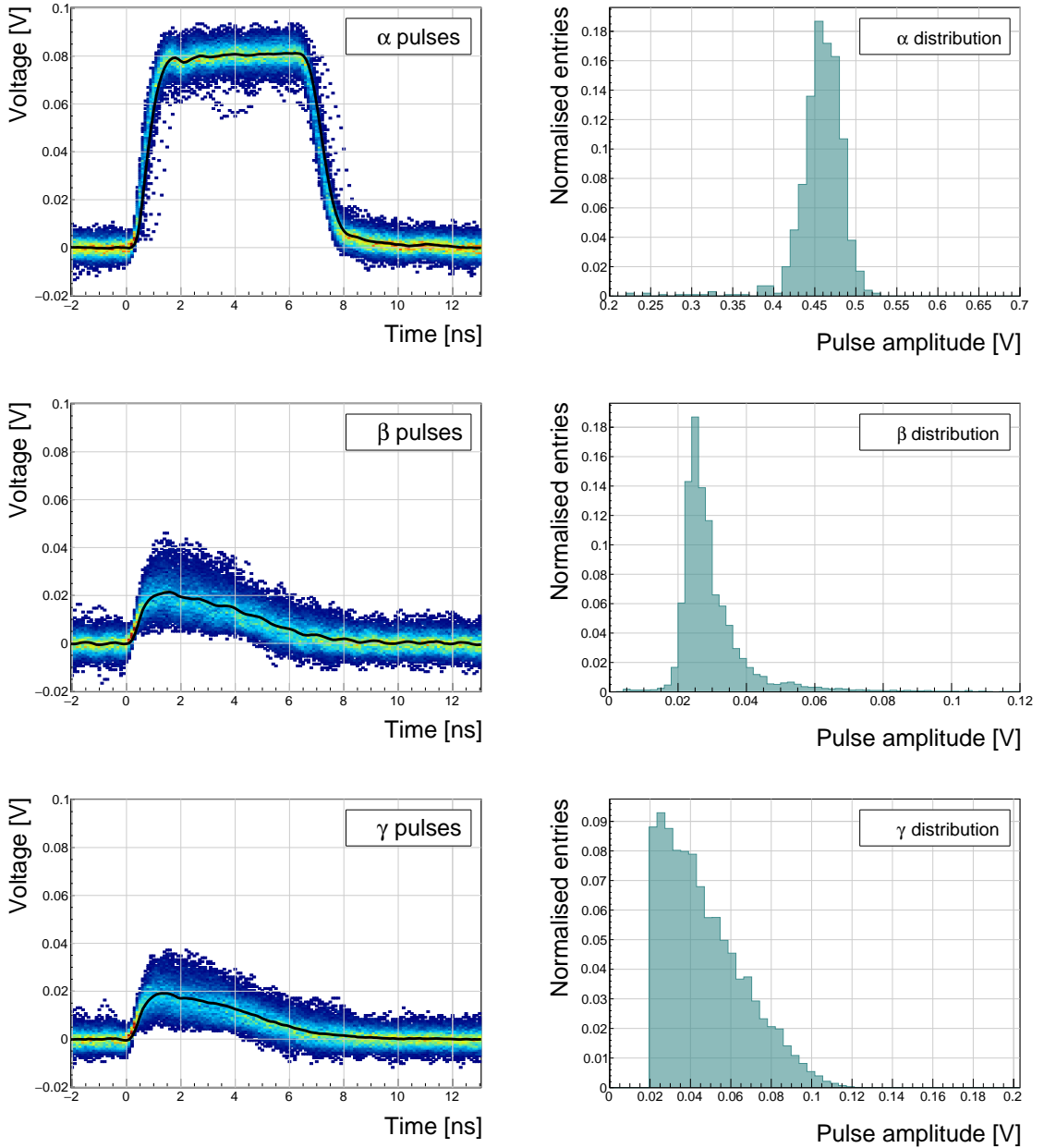


Figure 1.5: Superimposed and averaged pulses (left figures, current amplifier) and distributions of deposited energy (right figures, charge amplifier) for three types of radiation. Note the scale on the x axis of the distributions.

1.3. RADIATION LIMITATIONS

227 1.3 Radiation limitations

228 This section quantifies the decrease in charge collection efficiency as well as the effects on
229 long-term measurement stability in irradiated sCVD diamonds.

230 1.3.1 Irradiation study

231 This subsection contains a study of the effects of 300 MeV pion (π) irradiation on the charge
232 collection efficiency of sCVD diamond detectors. To carry out this study, two diamond
233 samples were irradiated with 300 MeV pions (π , kinetic energy 191.31 MeV). The irradiation
234 campaign took place at the Paul Scherrer Institute (PSI) [6] where the machine provides
235 a flux of $1.5 \times 10^{14} \pi \text{ cm}^{-2}$ per day. The quoted uncertainty on the measurement of the
236 delivered dose is $\pm 20\%$. In addition, a deviation in beam energy can have a significant
237 effect on the damage in the sensor, considering the pion damage curve in figure ?? at a
238 $\pi_{300 \text{ MeV}}$ point (191 MeV kinetic energy), which sits on a steep section of the DPA curve.
239 The target fluences for S79 and S52 were $(1 \pm 0.2) \times 10^{14} \pi \text{ cm}^{-2}$ and $(3.6 \pm 0.7) \times 10^{14} \pi \text{ cm}^{-2}$.

240 A test beam campaign was carried out to observe the charge collection efficiency at
241 different bias voltage settings. The efficiency values acquired are used to determine the
242 effective drop in efficiency as a function of fluence. This is to test if the collected charge Q
243 is inversely proportional to the fluence Φ . A procedure defined by a collaboration researching
244 diamond behaviour RD42 has been applied to the measured values to extract the damage
245 factor described in ??.

246 The following subsection contains measurements and results of a long-term stability
247 study using α and β particles. In particular, the charge collection efficiency with β and α
248 radiation as a function of time is measured. To investigate this effect on the scale of charge
249 carriers, the change of TCT (transient current technique) pulses with time is observed.
250 Finally, a procedure that improves the pulse shape and with it the charge collection is
251 proposed.

252 300 MeV π radiation damage factor

253 Three diamonds – non-irradiated S37 and irradiated S52 and S79 – were tested in a $\pi_{120 \text{ GeV}}$
254 test beam in the SPS North Experimental Area at CERN [7] before and after irradiation.
255 The goal was to estimate the charge collection efficiency and charge collection distance as a
256 function of fluence. The samples were primed prior to data taking using a ${}^{90}\text{Sr}$ radioactive
257 source. The data were then taken at a range of bias voltages ranging from 30 V to 900 V,
258 yielding between $0.06 \text{ V}/\mu\text{m}$ and $1.8 \text{ V}/\mu\text{m}$ electrical field in the bulk. Every data point
259 contained approximately 5×10^4 measured particles. The charge deposited by the particles
260 was measured using a CIVIDEC Cx charge preamplifier.

261 The integrated amplitude spectrum is a Landau distribution. Its most probable value
262 (MPV) is used to calculate the most probable collected charge Q_i :

$$Q_i [\text{e}^-] = \frac{1}{1.6 \times 10^{-19}} Q_i [\text{C}] = 6241 \cdot Q_i [\text{fC}] = 6241 \cdot \frac{\text{MPV} [\text{mV}]}{A [\frac{\text{mV}}{\text{fC}}]}, \quad (1.6)$$

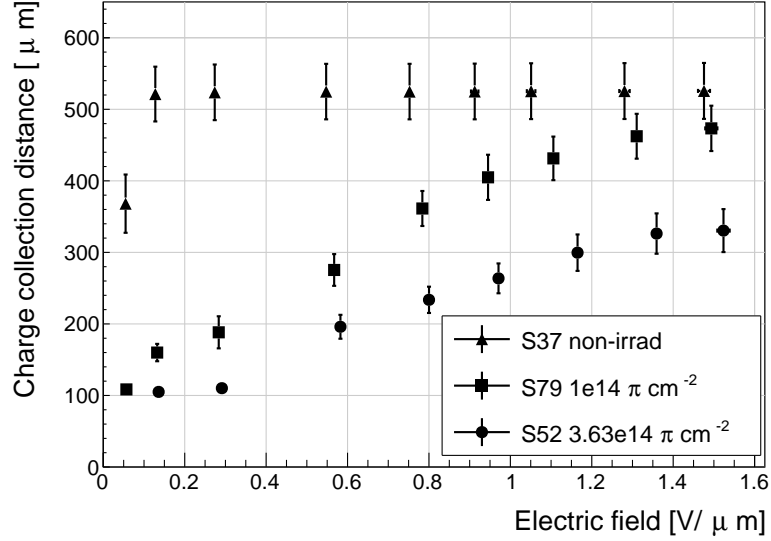


Figure 1.6: The figure shows the CCD for S37, S79 and S52 at a range of bias voltage settings.

263 where $A = 9.3 \text{ mV/fC}$ is the preamplifier gain factor and $1 e^- = 1.6 \times 10^{-19} \text{ C}$.

264 The CCD for the three measured samples at a bias voltages ranging from $0.2\text{--}1.6 \text{ V } \mu\text{m}^{-1}$
 265 calculated using equation ?? is shown in figure 1.6. S37 exhibits a full collection distance
 266 already at $0.4 \text{ V } \mu\text{m}^{-1}$ whereas the irradiated samples have a more gentle increase of CCD
 267 with increasing bias voltage. It is evident that at $1 \text{ V } \mu\text{m}^{-1}$ the maximum CCD has not
 268 been reached in the case of S79 and S52. Nevertheless, to compare the measured data point
 269 with those provided by RD42, the CCD at $1 \text{ V } \mu\text{m}^{-1}$ has to be taken.

270 The data points with the maximum CCD obtained in the test beam measurements are
 271 plotted as a function of fluence in figure 1.7. Equation ?? is fitted to the data points and
 272 a damage factor $k_\lambda = (4.4 \pm 1.2) \times 10^{-18} \text{ } \mu\text{m}^{-1} \text{ cm}^{-2}$ is obtained. The value is for a
 273 factor of two higher than the damage factor obtained by RD42. This could be due to an
 274 insufficient priming time ahead of the measurement. Figure 1.8 shows the effect of priming.
 275 The samples were only exposed to the radioactive source for a short time and might not
 276 have achieved the maximum charge collection. In addition, the diamond samples have not
 277 been polished and re-metallised after irradiation, as is the case for the RD42. A study of
 278 effects of re-metallisation on the charge collection is done in [8] and supports this theory.
 279 Finally, with only two samples measured, the statistical uncertainty is high. Nevertheless,
 280 it can be concluded that the 300 MeV pions damage the diamond bulk significantly more
 281 than the 24 GeV protons, as shown in chapter ??.

282 1.3.2 Long-term measurement stability

283 An important requirement for particle detectors is a stable performance over long periods
 284 of time. For instance, the charge collection for a defined radiation type and quantity must

1.3. RADIATION LIMITATIONS

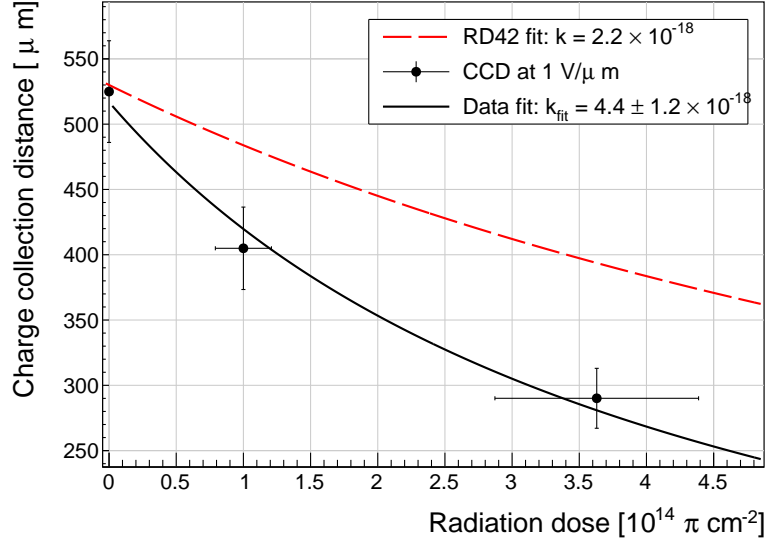


Figure 1.7: The charge collection distance at $1 \text{ V}/\mu\text{m}$ bias voltage for the three diamond samples is plotted as a function of fluence. It is compared to the RD42 data for pion irradiation. The data points are about 15–25 % lower than expected from the RD42 data [9].

not change over time or has to change in a predicted way. The stability of diamond detectors depends on many factors, e.g. material purity, polishing process, electrode material, irradiation damage etc. The aim is to study the behaviour of diamond under controlled conditions, with the goal to understand its limitations. One of these limitations is the fluence as it can affect the long-term stability of the sensor during operation.

The three diamond samples (S37, S79 and S52) have been exposed to two different types of ionising radiation for a longer period to see if their behaviour changes over time. Two parameters have been observed in particular:

1. Charge collection of β particles and
2. Charge collection and ionisation profile of α particles.

β long-term stability

The diamond samples have undergone a long-term stability test at room temperature using β radiation. This has been done using a ${}^{90}\text{Sr}$ source emitting $\sim 2.28 \text{ MeV}$ electrons at a rate of approximately $10^4 \text{ e}^- \text{ cm}^{-2}$. To simulate the initial conditions in HEP experiments, the sensors must not be primed before starting the measurements. The measurement setup consists of a diamond sample (S37, S52 or S79) with the CIVIDEC Cx spectroscopic amplifier, a silicon diode with a CIVIDEC C6 amplifier for triggering and a ${}^{90}\text{Sr}$ source on top. A particle emitted by the source traverses the sensor bulk and hits the silicon diode, triggering the analogue signal readout. The source is left on the top for the course of the experiment. The measurements, however, are taken at discrete times. For every data point, approximately 10^4 triggers have to be recorded. The offline analysis of the recorded signal

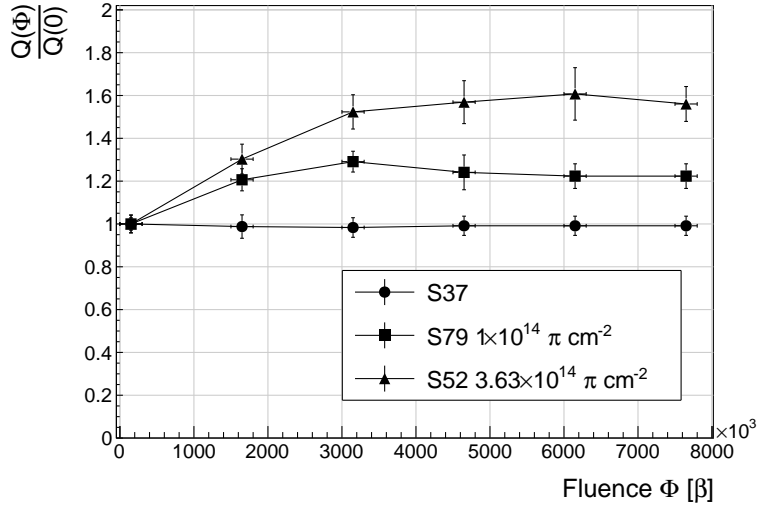


Figure 1.8: Relative increase of charge collection over time due to priming with the ^{90}Sr radioactive source. The charge collection for the non-irradiated S37 stays constant. The bias voltage for this measurement is $1 \text{ V}/\mu\text{m}$.

306 pulse amplitudes yields a Landau distribution for every data point. The current charge
307 collection relative to the initial charge collection for every sample is plotted as a function
308 of the received β dose in figure 1.8. It shows that, for the irradiated samples, the charge
309 collection efficiency improves when the diamond sensor is primed with a β source. The
310 effect is negligible for the non-irradiated high-quality S37. Both relative increases are sig-
311 nificant – 22 % for S79 and 55 % for S52. At a fluence of approximately 4×10^6 particles
312 the charge collection is stabilised. At that point S79 achieves close to a full efficiency (in
313 absolute values – not shown) whereas S52 reaches approximately 50 %.

314 To sum up, diamond provides a stable measurement of the β radiation detection after
315 reaching a stable state. Even if damaged by radiation, it reaches a stable charge collection
316 at a fluence of $\sim 4 \times 10^6$ MIPs. Its efficiency decreases with a high fluence. However, the
317 decrease can be accounted for if the damage factor and the rate and energy of the particles
318 are known. γ radiation has a similar impact on the diamond as the β . The incident
319 photons, if they interact with the diamond, prime the bulk, increasing the charge collection
320 efficiency. The difference, however, is that the interaction probability (cross-section) is lower
321 for gammas [10, 11].

322 α long-term stability

323 This part discusses the stability of irradiated diamond sensors during α measurements. An
324 ^{241}Am source has been used, emitting α particles with a mean energy of 5.5 MeV with an
325 average rate of 7 s^{-1} .

326 To test the stability of the diamond during α measurements, the samples have been
327 biased at $+500 \text{ V}$ and exposed to up to $8 \times 10^3 \alpha$ hits while measuring their charge collection

1.3. RADIATION LIMITATIONS

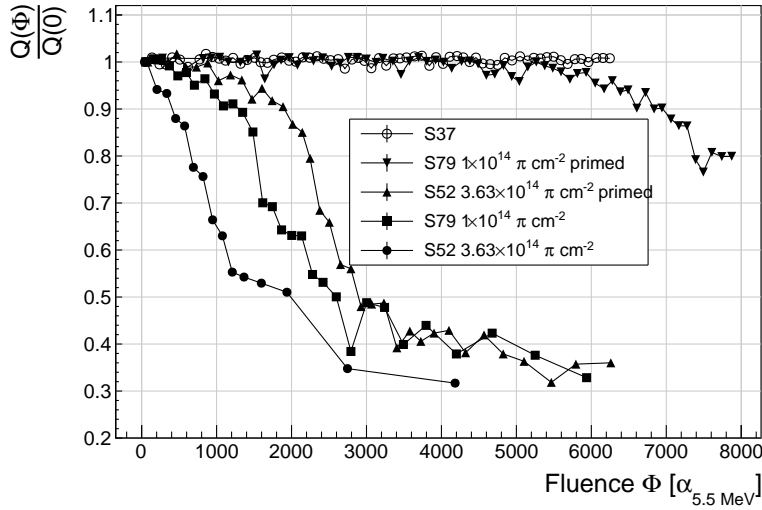


Figure 1.9: A relative drop in charge collection efficiency as a function of the received α dose for non-irradiated and irradiated diamond samples.

efficiency using the CIVIDEC Cx spectroscopic amplifier. The charge collected at every measurement point $Q(\Phi)$ is compared to collected charge of the first measurement $Q(0)$. The resulting ratio $\frac{Q(\Phi)}{Q(0)}$ for all samples is shown in figure 1.9. Each measurement point is an average of 30 consecutive α hits. The observations are the following:

- $Q(\Phi)$ for the non-irradiated S37 is stable as compared to $Q(0)$ over the course of the measurement.
- The initial efficiency of the irradiated S52 and S79 starts decreasing already at a low α count.
- The charge collection efficiency of the unprimed irradiated samples drops much faster than after priming.
- The particle count rate decreases with decreased efficiency, which is clearly seen in the unprimed S52 data where the data points at a low efficiency are much further apart.

The absolute values are not shown here because only the relative drop is of interest in the scope of the long-term stability tests.

To investigate this sudden drop in efficiency, the current pulse shapes using a CIVIDEC C2 current amplifier have to be observed, as shown in figure 1.10. The shape of the pulse holds more information about the charge carrier properties in the sensor than solely the value of the integrated charge. This time only the primed S79 sample has been tested. Both the hole and the electron collection are observed to determine whether they behave differently or not.

The first observation in the raw acquired data in figures 1.10 is that the initially stable

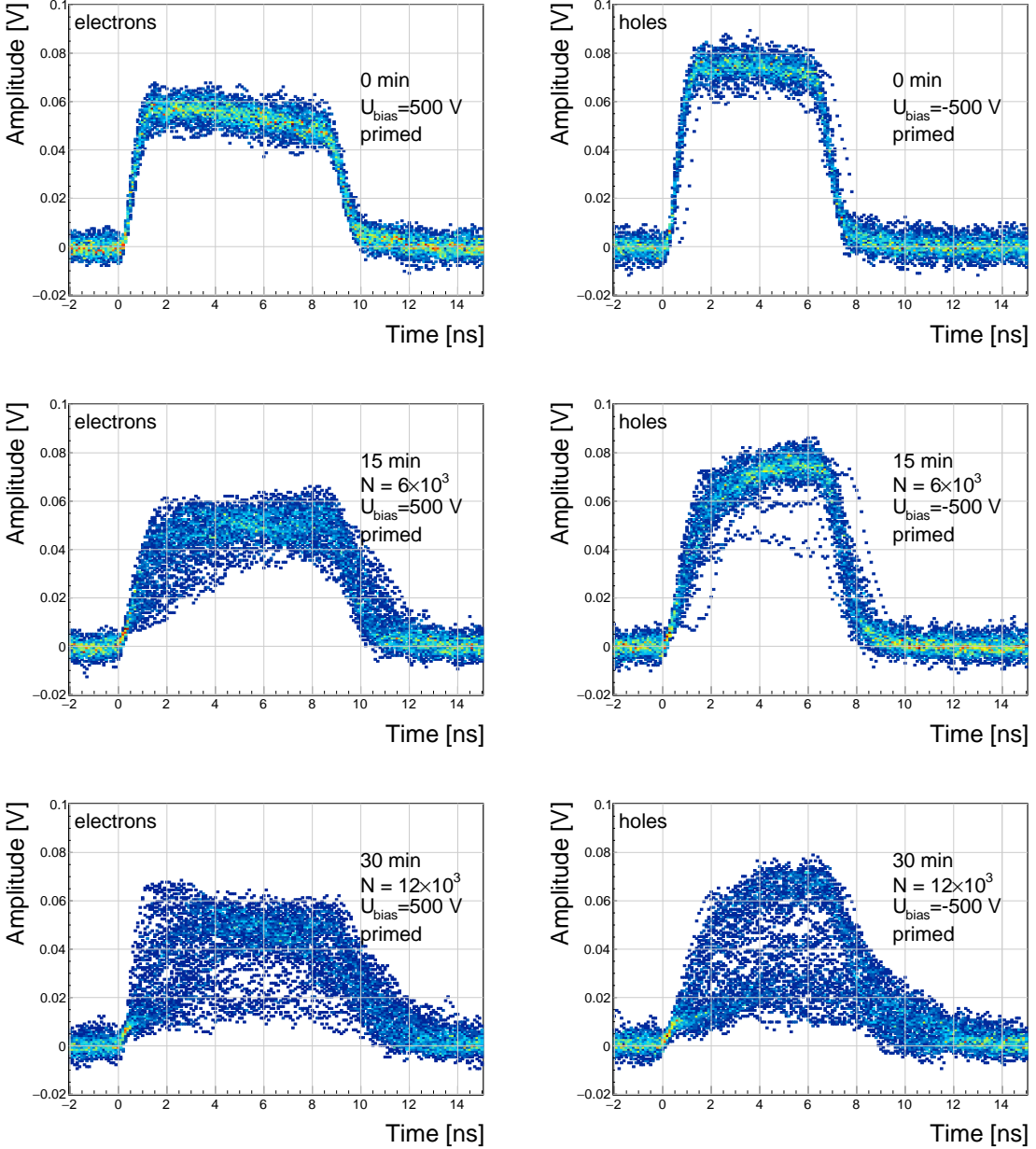


Figure 1.10: The signal of the irradiated and primed S79 deteriorates with time for both polarities. Every plot contains 60 superimposed pulses.

349 pulses start deteriorating; several different shapes start appearing gradually, some still very
 350 similar to those from the beginning while the others with almost zero amplitude.

351 A more dedicated analysis of the first observation has been carried out as follows: at
 352 the beginning of the test when the diamond is still operating stably, 60 pulses are recorded.
 353 An average pulse is calculated. This is a reference pulse for the subsequent measurement
 354 points. Then an RMS of the individual pulses σ_n with respect to the reference pulse is

1.3. RADIATION LIMITATIONS

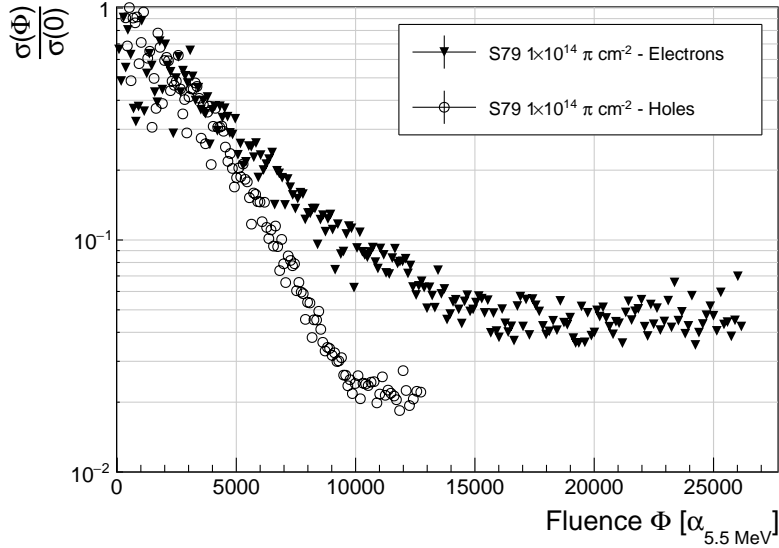


Figure 1.11: Deterioration of the pulse shapes with time.

355 calculated and the resulting RMS values are summed together into $\sigma(0)$:

$$\sigma(0) = \sum_{n=1}^{60} \sigma_n. \quad (1.7)$$

356 All the subsequent data points also consist of a set of 60 pulses. At every data point the
 357 summation of the RMS values of the individual pulses with respect to the initial averaged
 358 pulse σ is calculated according to equation 1.7. The ratio between the initial $\sigma(0)$ and
 359 discrete values σ gives a measure of the change of the pulse shape with respect to the
 360 reference pulse at the start of the measurement. Therefore the initial value is 1 and it
 361 decreases if the RMS values of subsequent data points are higher. Figure 1.11 shows the ratio
 362 $\frac{\sigma(\Phi)}{\sigma(0)}$. From the data obtained it can be concluded that the initial pulse shape quickly starts
 363 deteriorating. In fact, the deterioration of the shape follows an approximate exponential
 364 decay function, which can be fitted to the data. The resulting decay constants for electrons
 365 and holes are $\tau_e = (4400 \pm 150) \alpha^{-1}$ and $\tau_h = (3300 \pm 140) \alpha^{-1}$. The electrons retain the
 366 initial shape for longer. The deteriorated shapes also seem to be for a factor of 2 better
 367 than those of the holes.

368 **Discussion** One hypothesis is that this behaviour is caused by space-charge build-up.
 369 Charge carriers get stopped in the charge traps in the bulk for a long time, building up
 370 regions of space-charge. The built up space-charge affects the electric field. The field in
 371 turn affects the speed of the drifting charge carriers. Since the movement of the carriers is
 372 inducing the electric current, the field gradient can be observed in the current signal. The
 373 fact that the signal shapes vary significantly might be due to a very non-uniform electric
 374 field. Figure 1.12 shows how the space-charge might be built up at the entry point of the
 375 α particle. The assumption is that the first 3 μm of diamond surface are significantly more

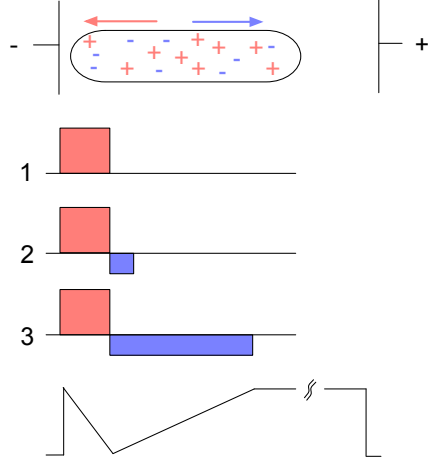


Figure 1.12: Space-charge build-up at the electrode.

damaged than the rest of the material. Therefore the probability that charge carriers would get trapped at the edge of the sensor is higher. If the sensor is biased as shown in the figure, the positive charge cloud drifts towards the adjacent electrode while the negative cloud drifts through the sensor to the opposite one. Therefore most of the trapped carriers at the adjacent electrode are positive, forming a strong positive space-charge in the first few μ of the sensor (1). The negative carriers created by subsequent α particles are attracted by the positive space charge and get trapped close to the positive space-charge (2). This negative space-charge region is gradually stretched inwards (3). Together the two regions form a barrier which counteracts the externally applied electrical field. Such a distortion of the field prevents the charge carriers from drifting freely within the space-charge region. Only those negative carriers that diffuse through this barrier can start drifting towards the positive electrode. Others either recombine or are trapped, contributing to the build-up of the barrier.

This hypothesis explains the gradual loss of collected charge in figure 1.9 and the pulses with a slow rising edge in figures 1.10. However, it cannot explain the electron pulses with a negative slope. Further reading regarding the space-charge build-up is available in [12, 13, 14].

Restoring the pulse shapes Finally, an effort has been made to find a way for the pulse shapes to return to their initial state. Five methods are listed:

- 395 1. No source, with bias voltage,
- 396 2. No source, without bias voltage,
- 397 3. Priming with γ at a rate of $400 \text{ s}^{-1}\text{cm}^{-1}$ without bias voltage,
- 398 4. Priming with β at a rate of $1000 \text{ s}^{-1}\text{cm}^{-1}$ with bias voltage and
- 399 5. Priming with β at a rate of $1000 \text{ s}^{-1}\text{cm}^{-1}$ without bias voltage.

1.3. RADIATION LIMITATIONS

400 Before starting each method, the diamond sample S79 is first primed using a ^{90}Sr source for
401 approximately one hour. Then the bias voltage is switched on and an ^{241}Am source is put
402 on top. The pulses produced by the incident α particles have a proper rectangular pulse
403 at the beginning, but then start changing – first gradually and later increasingly more in
404 an erratic way, as described in the text above. After approximately 30 minutes, one of the
405 methods is tested. When a “healing” procedure is started, a set of 60 pulses is taken at
406 irregular points of time to observe the change in the pulse shape and to assess the quality
407 of the “healing” procedure. Then the bias voltage is switched off and the sample is primed
408 again to reset its state before starting with the next run.

409 The results depicted in figure 1.13 show that the methods (3) and (5) improve the shape,
410 method (2) helps slowly, (1) does not show any change with time and (4) at first improves,
411 but then significantly degrades the shape. The effect observed in method (4) has already
412 been described in [15]. The “healing” process therefore depends on the rate of radiation,
413 the bias voltage and the time of exposure. The ionising radiation creates free charges, which
414 quickly recombine close to the place of generation. It is likely that they also release the
415 charges trapped during the measurement, reducing the overall effect of the space-charge.
416 The traps get filled with both flavours of carriers, thus they are neutralised. The pulse
417 shape gradually returns to its initial state.

Procedure	Source	Type of radiation	Bias voltage	Effectiveness
1	/	/	ON	no
2	/	/	/	slow
3	^{60}Co	γ	/	YES
4	^{90}Sr	β	ON	no
5	^{90}Sr	β	/	YES

419 Table 1.2: Effectiveness of healing procedures.

420 **Summary** The shape of the pulses caused by α radiation changes with time for irradiated
421 samples. The shape of the pulses gets distorted and becomes erratic. The charge collection
422 decreases and its spread increases. The signal shapes are probably affected by a non-uniform
423 electric field, which is caused by the build-up of space charge. The signal degradation
424 happens even faster for non-primed diamonds. To “heal” the diamond – to bring the pulse
425 shapes back to their initial shape – the sample must be primed using a β or a γ source for
426 several minutes without bias voltage. Switching to the inverse polarity for a few seconds
427 helps a bit, but in a long run distorts the signal, preventing it from returning to the initial
428 shape.

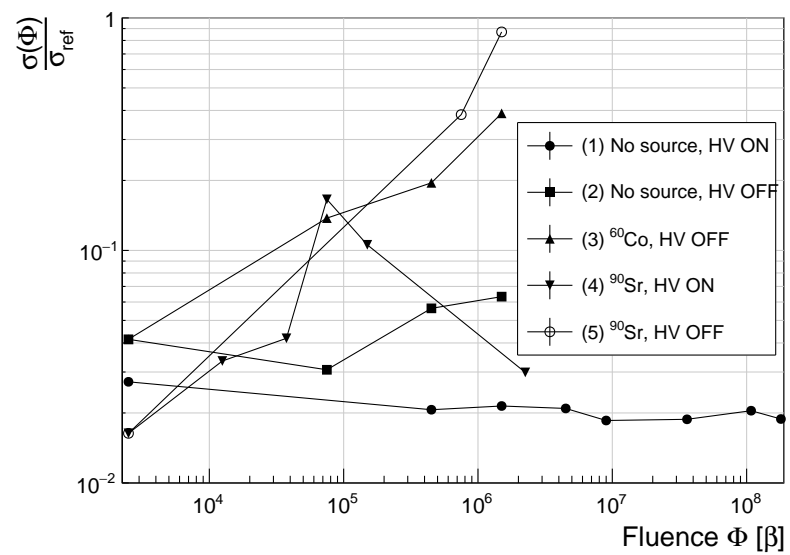


Figure 1.13: Comparison of the five procedures for the “healing” process for an irradiated diamond that had been exposed to α radiation with a rate of 10^1 s^{-1} , with the bias voltage switched on, for at least 30 minutes.

1.4. TEMPERATURE LIMITATIONS

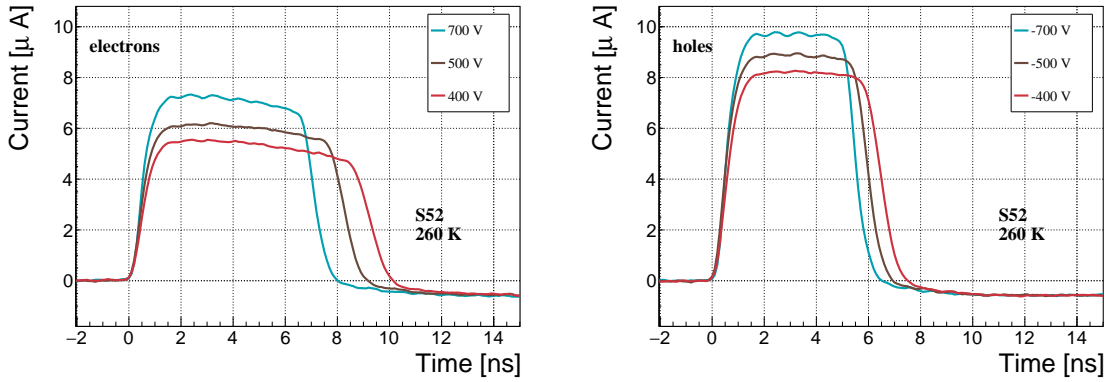


Figure 1.14: Varied bias voltage at a fixed temperature.

429 1.4 Temperature limitations

430 A test has been carried out to evaluate the effect of temperature changes on the output
 431 signal of the diamond sensors. A cryostat filled with liquid helium is used to cool down
 432 the sensor during the measurement process. The current signal response to α -particles is
 433 measured at 18 temperature points between 4 K and 295 K. At every temperature point
 434 a set of 300 pulses is recorded at various bias voltages. The resulting data show that the
 435 charge collection is stable from RT down to 150 K where it starts decreasing. It stabilises
 436 again at about one third of the initial value at 75 K. This behaviour was first measured and
 437 discussed by H. Jansen [5].

438 1.4.1 Temperature-variant α -TCT before irradiation

439 Three sCVD diamond samples have been tested at a range of temperatures using the α -
 440 TCT technique. At each temperature point, the bias voltage is set to several positive and
 441 negative values. A set of 300 pulses is recorded at every data point and averaged offline.
 442 The resulting averaged pulses of sample S37 at the 260 K temperature point and a bias
 443 voltage of ± 700 V, ± 500 V and ± 400 V are shown in figure 1.14. The pulses induced by
 444 holes as charge carriers are shorter than those induced by electrons, which means that holes
 445 travel faster in diamond. The area of the pulse, however, is the same for both polarities,
 446 which corresponds to the fact that the same amount of charges is drifting in both cases.

447 Figure 1.15 shows pulses at a bias voltage set to ± 500 V across the range of tempera-
 448 tures between 4 K and 295 K. Several conclusions can be drawn by observing their shape.
 449 First, the pulse shapes change with decreasing temperature. The pulse time gets shorter
 450 and higher, hinting at the faster carrier drift velocity v_{drift} . Second, between 150 K and
 451 75 K there is a significant change in shape - the time constant of the rising edge increases
 452 significantly and the pulse area decreases. From 75 K down to 4 K there is no significant
 453 change. Last, the top of the pulse at the S52 is not flat, which means that a portion of
 454 the drifting charge is lost along the way. This is due to charge trapping, likely by means of

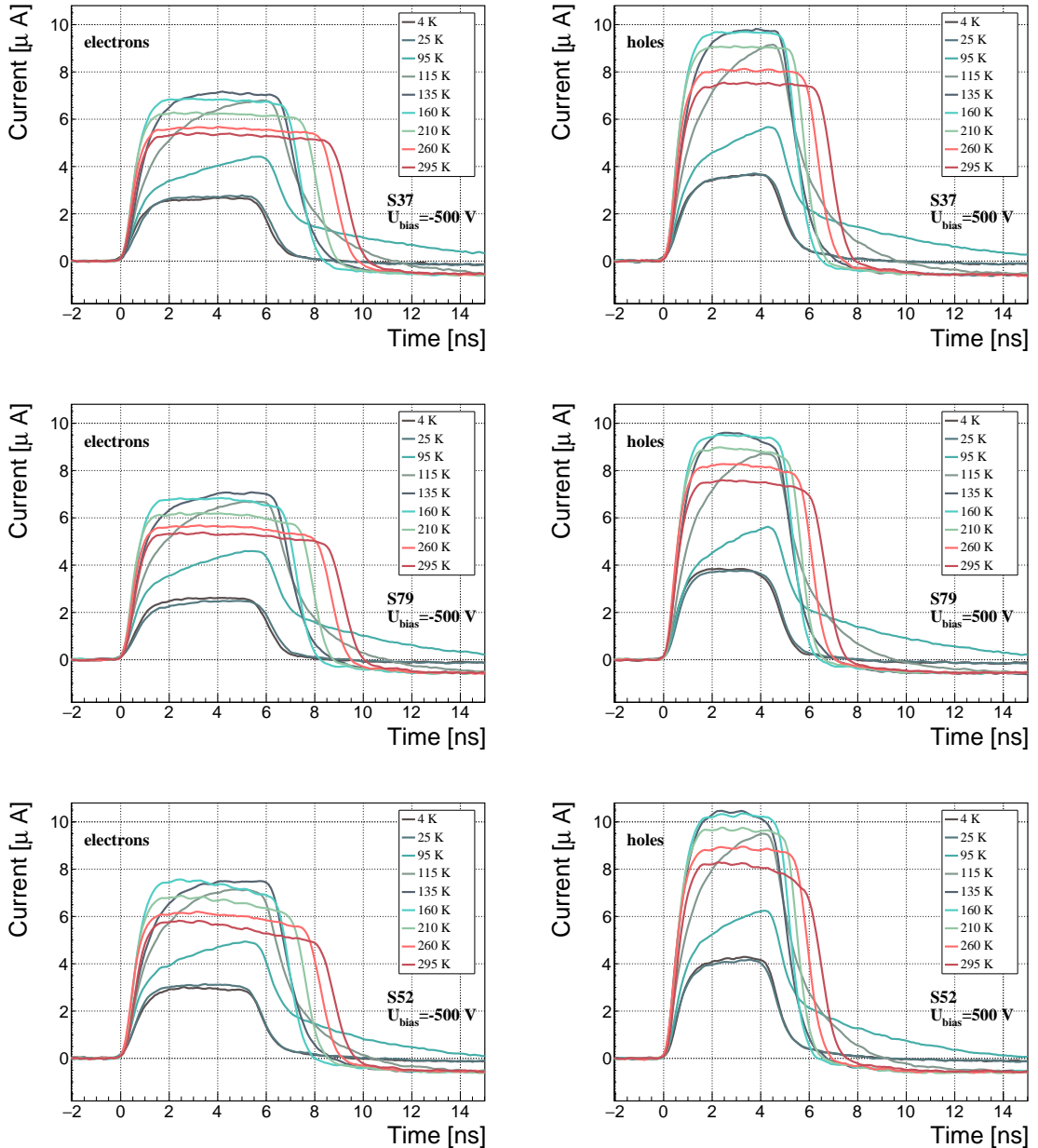


Figure 1.15: Several data points between 4 K and 295 K at a bias voltage of ± 500 V. The tilted top of the pulse on the bottom left figure is due to built-up space charge.

1.4. TEMPERATURE LIMITATIONS

455 crystal defects or impurities.

456 1.4.2 Temperature-variant α -TCT after irradiation

457 The irradiated S79 and S52 have been re-tested in the cryostat after irradiation. The aim
458 is to observe how their pulse shapes change with decreasing temperature, in particular the
459 decaying top of the pulses, as shown in figure 1.16. The decay time gives information on
460 trapping of charge carriers while travelling through the diamond bulk. A variation of the
461 decay time constant as a function of temperature might help to reveal the type and depth
462 of the charge traps. To observe these effects or lack thereof, a number of requirements
463 have to be met. First, the diamond samples are intentionally not primed prior to the
464 experiment because priming would improve the pulse shapes and possibly change the decay
465 time constant of the signal. Second, keeping in mind that the pulse shape of irradiated
466 diamonds changes with time, the duration of the measurement of an individual data point
467 has to be short – of the order of 30 seconds. Last, the sequence of the bias voltage settings
468 is important, the reason for which is explained below.

469 Unfortunately it is not possible to avoid temporal pulse changes. For instance, one
470 measurement point takes approximately one minute. After the measurement, the bias
471 voltage polarity is swapped for a few seconds to bring the diamond back into its initial state.
472 But a few seconds with respect to a minute are not enough, but due to time constraints
473 this cannot be avoided. Therefore when the bias voltage is set to the next value, there is
474 still some residual effect of the previous measurement. Similar to the effects of polarisation,
475 this effect is also decreasing the pulse height. This can be observed in figure 1.16, which
476 shows the resulting pulses of S52 for bias voltages of ± 200 V, ± 300 V, ± 400 V and ± 500 V
477 at 230 K and 260 K. In this case the measurement sequence is: 230K (200 V, 300 V, 400 V,
478 500 V, -500 V, -400 V, -300 V), 260 K (-200 V, -300 V, -400 V, -500 V, 500 V, 400 V,
479 300 V). The changes in pulse shapes for holes at 230 K and 260 K cannot be attributed to
480 the temperature change. Instead, the explanation could lie in diamond “polarisation”. This
481 means that, when exposed to an electric field with α measurements ongoing, an internal
482 electric field of inverse polarity builds up in the diamond, which effectively reduces the
483 overall electric field. This internal field does not dissipate when the external bias voltage
484 is switched off. The diamond becomes “polarised”. When switching the polarity of the
485 external bias voltage, the internal and external electric field point in the same direction at
486 the beginning, increasing the overall electric field and with it the pulse height. In figure 1.16
487 this happens when switching from 500 V (figure 1.16a) to -500 V (figure 1.16b) at 230 K.
488 The built up polarisation contributes to the pulse having a sharp rising edge and a high
489 amplitude. This effect decays during the next two voltage points. There would be a handful
490 of ways to avoid this polarisation effect in the data:

- 491 1. After every data point invert the bias voltage and leave it to return to a neutral state
492 for the same amount of time,
- 493 2. Make a hysteresis of data points, going from minimum negative to maximum positive
494 bias several times,

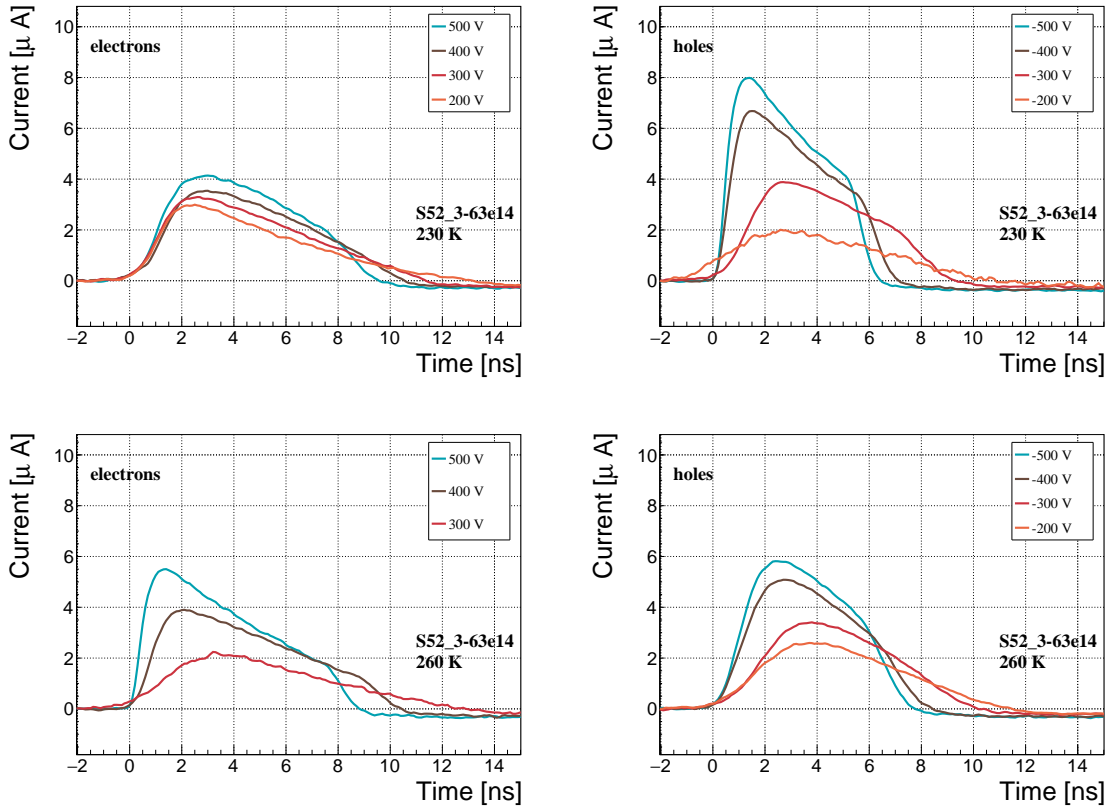


Figure 1.16: Varied bias voltage at a fixed temperature for an irradiated sample.

495 3. Reduce the measurement time at every bias voltage setting.

496 Unfortunately, options (1) and (2) are very time consuming and would increase the overall
497 experiment time to over one day. The third option would worsen the resulting averaged
498 pulses. In the end an alternative option has been chosen: alternating the starting bias
499 voltage and the sequence at every temperature point. With this option, a meaningful
500 systematic error in analysing the pulse shapes can be attained.

501 Figure 1.17 shows the irradiated S52 and S79 as well as the non-irradiated S37 for
502 comparison, all at a bias voltage of ±500 V and at several temperature points between 4 K
503 and 295 K. It is evident that the radiation damage affects the shape of the pulses across all
504 temperatures.

505 **Collected charge as a function of temperature**

506 The collected charge as a function of temperature for electrons and holes is plotted in
507 figures 1.18 and 1.19, respectively. In the framework of this thesis the focus is on the
508 effect in the irradiated devices. The new contribution are the data points for the irradiated
509 samples. The focus is on the temperature range between 4–75 K and 150–295 K whereby
510 the effect of the re-excitation of bound electrons and holes is not prevailing. The values

1.4. TEMPERATURE LIMITATIONS

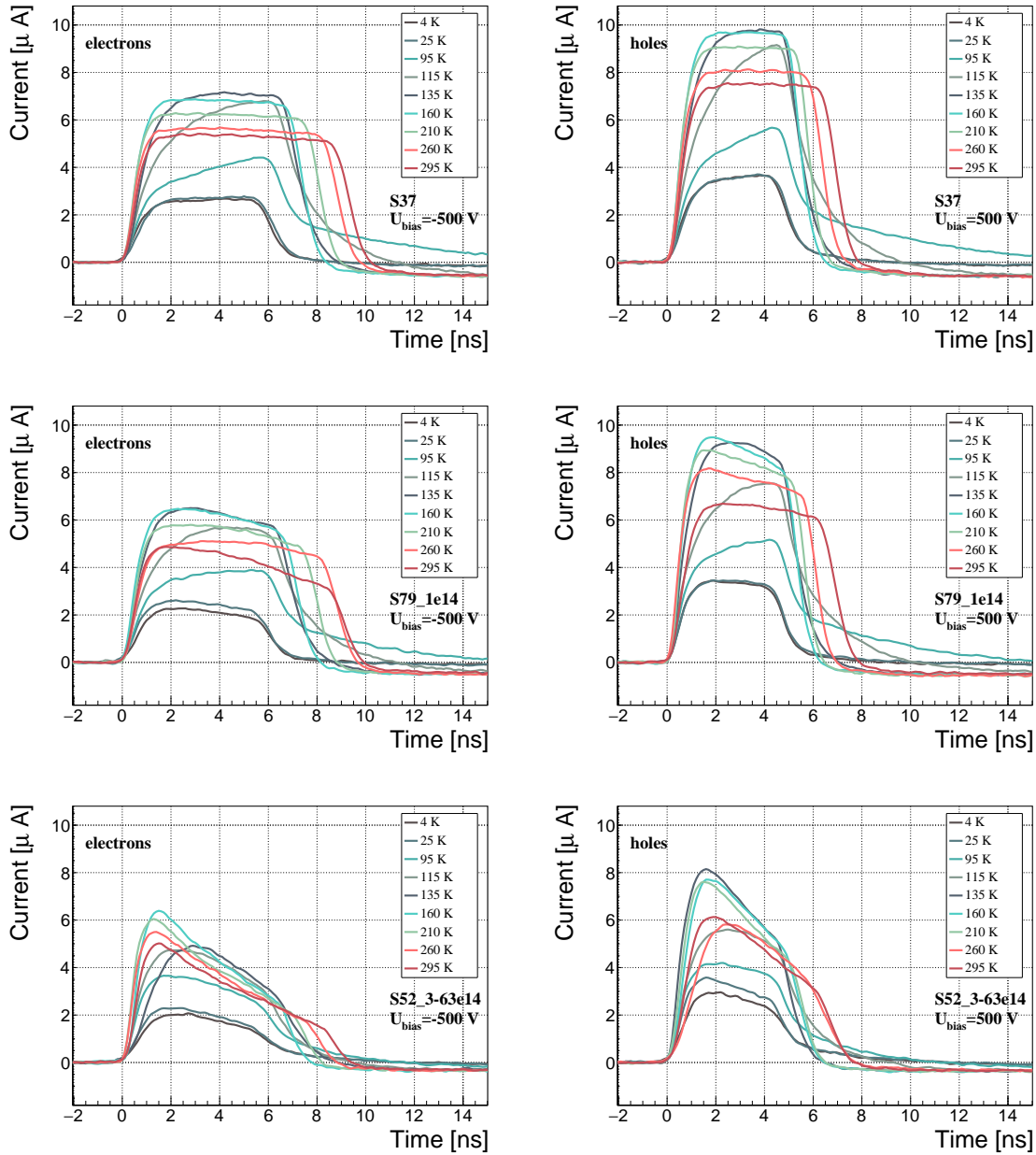


Figure 1.17: After irradiation: several data points between 4 K and 295 K at a bias voltage of ± 500 V.

for all samples are fairly stable in the range between 4 K and 75 K and between 150 K and 295 K. However, in the values for the irradiated S52 some excursions can be observed. This is due to the sequence of the measurement steps, which results in a hysteresis effect explained in the preceding text.

The collected charge drops significantly from 150 K down to 75 K. In the non-irradiated samples the values in the lower temperature range are approximately 30 % of those in the high range. For the irradiated samples this difference is lower: 35 % for S79 and 50 % for

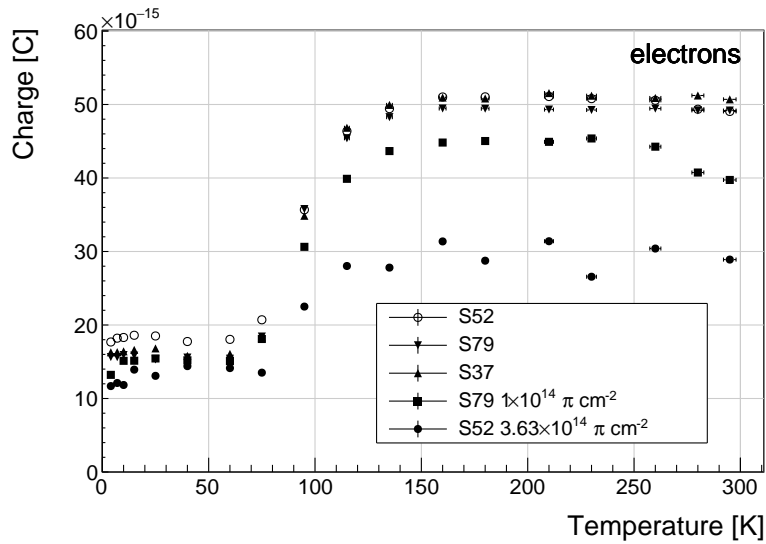


Figure 1.18: Collected charge for electrons as a function of temperature.

518 S52.

519 An interesting detail in figure 1.18 is that the ratio between the values for non-irradiated
520 samples and their irradiated counterparts at the lower temperature range is different than
521 at the higher range. In other words, the charge loss due to irradiation damage is lower for
522 temperatures between 4 K and 75 K than for temperatures between 150 K and 295 K. The
523 irradiated S52 collects 78 % of the initial charge in the low temperature range, but only
524 59 % of the initial charge for the high range. The values for S79 for these two temperature
525 ranges are 100 % and 90 %, meaning that the drop in charge collection efficiency after
526 irradiation to $1 \times 10^{14} \pi \text{ cm}^{-2}$ is negligible for temperatures below 75 K.

527 **Charge trapping**

528 A decaying exponential function from equation ?? has been fitted to the decaying top of the
529 averaged pulses at a bias voltages of $\pm 400 \text{ V}$ and $\pm 500 \text{ V}$ across all temperatures excluding
530 the transitional range between 75 K and 150 K. The resulting decay time constants τ are
531 effective carrier trapping times. The values differ for individual temperature points due to
532 changing pulse shapes with time by means of “polarisation”. This counts as a systematic
533 error. Therefore the fitted τ for $\pm 400 \text{ V}$ and $\pm 500 \text{ V}$ are averaged into one value representing
534 the measurement at that temperature point. The time constants should be infinite for an
535 ideal and non-irradiated sample.

536 As seen in figures 1.20a and 1.20b, the fitted values of the irradiated samples are fairly
537 stable across all temperatures. There is a slight increase in the decay time constant of the
538 S52 from $(6.0 \pm 0.5) \times 10^{-9} \text{ s}$ above 150 K to $(8.5 \pm 0.9) \times 10^{-9} \text{ s}$ below 75 K. This step is
539 however not observable in the S79 data. With only one sample exhibiting this behaviour,
540 the effect is not significant. Judging by the data acquired, the samples would need to be

1.4. TEMPERATURE LIMITATIONS

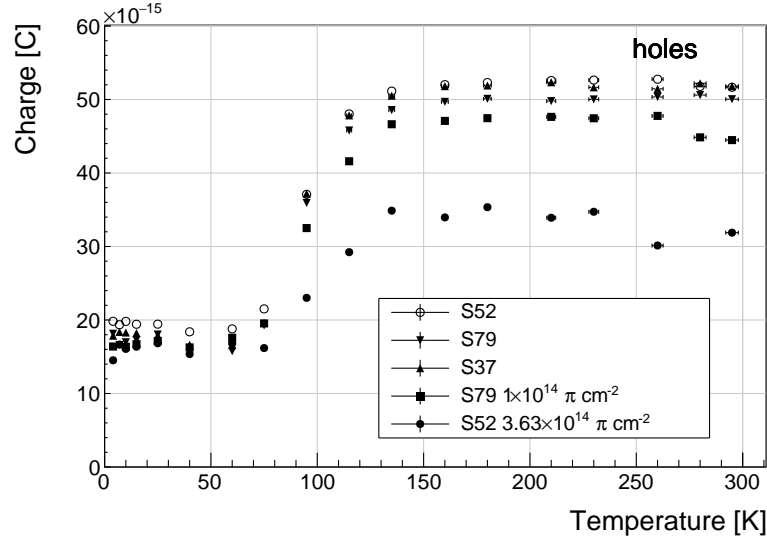


Figure 1.19: Collected charge for holes as a function of temperature.

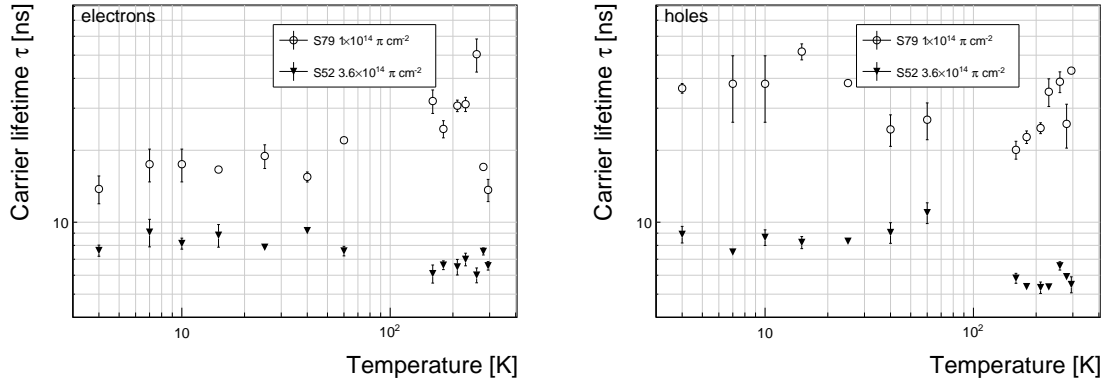


Figure 1.20: Charge carrier lifetime as a function of temperature for electrons and holes at ± 400 V and ± 500 V. The data points between 75 K and 150 K are omitted.

irradiated to doses above $5 \times 10^{14} \pi \text{ cm}^{-2}$ to quantify this effect in detail. Building on this assumption, the conclusion is that the signal decay time constant for irradiated sCVD diamond is constant across the temperature range between 4 K and 295 K, excluding the transitional range between 75 K and 150 K where it cannot be quantified properly. All things considered, the values can be averaged into one single effective trapping time value for electrons and one for holes for further analysis. The effective trapping time is inversely proportional to the fluence [16]:

$$\frac{1}{\tau} = \beta \cdot \Phi \quad (1.8)$$

where β is the proportionality factor. A low β value would mean that the trapping centres in the sensor are created with a low rate. Figure 1.21 shows the inverse trapping times of the non-primed irradiated samples as a function of $\pi_{300 \text{ MeV}}$ fluence. β is the slope

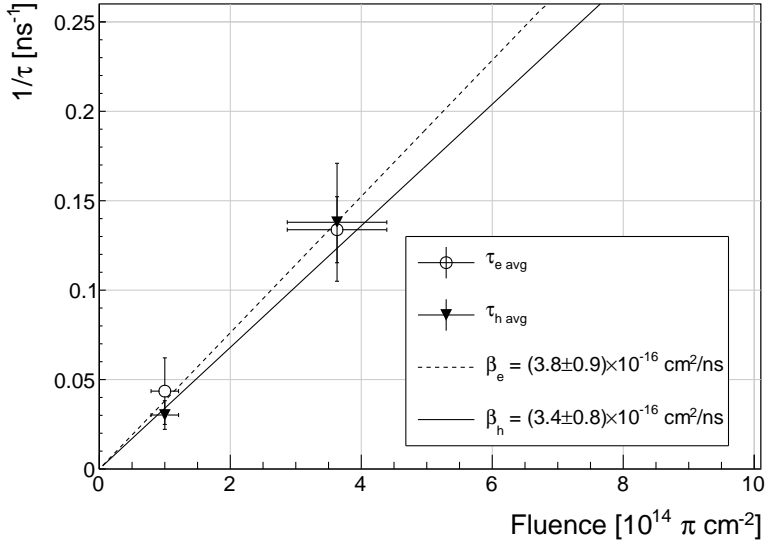


Figure 1.21: This figure shows the inverse charge trapping times averaged over all temperatures and plotted as a function of the π fluence.

of the fitted linear function. The fitted factors are $\beta_e = (3.8 \pm 0.9) \times 10^{-16} \text{ cm}^2/\text{ns}$ and $\beta_h = (3.4 \pm 0.8) \times 10^{-16} \text{ cm}^2/\text{ns}$. Comparing to silicon detectors in [16], the value for the sCVD diamond is two times lower.

1.5 Conclusion

This chapter gives an overview of the capabilities and limitations of diamond as a particle detector. Two effects on diamond are studied – radiation and temperature.

Two sCVD diamond detectors were irradiated with 300 MeV pions. They were tested alongside a non-irradiated sample to observe the changes in the ability to detect α , β and γ radiation. Their charge collection efficiency was measured in a test beam facility. The results were compared to the results from the RD42 collaboration and a DPA model. A radiation damage factor $k_\lambda = (4.4 \pm 1.2) \times 10^{-18} \mu\text{m}^{-1} \text{ cm}^{-2}$ was obtained for $\pi_{300 \text{ MeV}}$ particles. The data point was not in agreement with the data provided by RD42 nor with the model. However, the irradiation process and the low number of tested samples hold a relatively high statistical uncertainty. In addition, there was no diamond surface treatment done in between the measurements, as is the case in the study conducted by RD42. The results obtained in the course of these measurements are going to be fed into the existing pool of data in the RD42 collaboration.

The next step was to test the long-term capabilities for α detection. The shape of the ionisation profile was investigated to determine the behaviour of the charge carriers in the irradiated diamond. An exponential decay was observed in the pulses of irradiated samples, proving that there are charge traps in the bulk that were created during irradiation. Then a long-term stability test was carried out. The results show that the irradiated diamond

1.5. CONCLUSION

detectors do not provide a stable and reliable long-term measurement of α particles. This might be due to a space-charge build-up in the bulk, which changes the electric field, affecting the charge carriers. A procedure to improve the pulse shape using β and γ radiation was proposed.

Finally, the diamond sensors were cooled down to temperatures between 4 K and 295 K. Their response to α particles was observed. The results of the non-irradiated and irradiated samples were compared. The effect of reduction for the number of drifting charges due to exciton recombination was observed in both sets of data. The second set had a superimposed effect of charge trapping during the drift, which was represented by an exponential decay in the signal. The decay time constant did not change with temperature. Therefore all temperature points for individual samples were averaged and the decay time constants were plotted as a function of fluence. Proportionality factors for defect production rate $\beta_e = (3.8 \pm 0.9) \times 10^{-16} \text{ cm}^2/\text{ns}$ and $\beta_h = (3.4 \pm 0.8) \times 10^{-16} \text{ cm}^2/\text{ns}$ for non-primed diamonds were extracted.

⁵⁸⁷ Bibliography

- 588 [1] *Element Six*. <http://www.e6.com>.
- 589 [2] *IHa Technologies Pte. Ltd.* <https://www.2atechnologies.com>.
- 590 [3] M. Červ, P. Sarin, H. Pernegger, P. Vageeswaran, and E. Griesmayer. *Diamond de-*
591 *tector for beam profile monitoring in COMET experiment at J-PARC*. *Journal of*
592 *Instrumentation*, 10(06):C06016, 2015.
- 593 [4] *DRS4*. <https://www.psi.ch/drs/evaluation-board>.
- 594 [5] Hendrik Jansen, Norbert Wermes, and Heinz Pernegger. Chemical Vapour Deposition
595 Diamond - Charge Carrier Movement at Low Temperatures and Use in Time-Critical
596 Applications. PhD thesis, Bonn U., Sep 2013. Presented 10 Dec 2013.
- 597 [6] *Paul Scherrer Institute*. <https://www.psi.ch/>.
- 598 [7] Giorgio Brianti. SPS North Experimental Area. Technical Report CERN-SPSC-T-73-8.
599 LabII-EA-Note-73-4, CERN, Geneva, 1973.
- 600 [8] Michal Pomorski. Electronic properties of single crystal cvd diamond and its suitability
601 for particle detection in hadron physics experiments. *Wolfgang von Goethe University,*
602 *Frankfurt am Main, Germany*, 2008.
- 603 [9] M. Mikuž. *Diamond sensors for high energy radiation and particle detection*. TIPP,
604 2011.
- 605 [10] V. Sarin. Comprehensive Hard Materials. Elsevier Science, 2014. p. 411.
- 606 [11] E. Griesmayer and B. Dehning. *Diamonds for Beam Instrumentation*. Physics Procedia,
607 37:1997 – 2004, 2012. Proceedings of the 2nd International Conference on Technology
608 and Instrumentation in Particle Physics (TIPP 2011).
- 609 [12] V Eremin, E Verbitskaya, and Z Li. Effect of radiation induced deep level traps on si
610 detector performance. *Nuclear Instruments and Methods in Physics Research Section*
611 *A: Accelerators, Spectrometers, Detectors and Associated Equipment*, 476(3):537 – 549,
612 2002. Proc. of the 3rd Int. Conf. on Radiation Effects on Semiconductor Materials,
613 Detectors and Devices.

BIBLIOGRAPHY

- 614 [13] S. F. Kozlov, R. Stuck, M. Hage-Ali, and P. Siffert. Preparation and characteristics of
615 natural diamond nuclear radiation detectors. *IEEE Transactions on Nuclear Science*,
616 22(1):160–170, Feb 1975.
- 617 [14] Eugenijus Gaubas, Tomas Ceponis, Dovile Meskauskaitė, and Nikolai Kazuchits. Pro-
618 filing of current transients in capacitor type diamond sensors. *Sensors*, 15(6):13424,
619 2015.
- 620 [15] Gregor Kramberger, V. Cindro, A. Gorisek, I. Mandic, M. Mikuz, and M. Zavrtanik.
621 *Effects of bias voltage during priming on operation of diamond detectors*. PoS, Ver-
622 tex2012:013, 2013.
- 623 [16] Alison G. Bates and Michael Moll. A comparison between irradiated magnetic czechral-
624 ski and float zone silicon detectors using the transient current technique. *Nuclear In-
625 struments and Methods in Physics Research Section A: Accelerators, Spectrometers,
626 Detectors and Associated Equipment*, 555(12):113 – 124, 2005.